Event-based contact angle measurements inside porous media using time-resolved micro-computed tomography

Arjen Mascini[1], Veerle Cnudde[1,2] & Tom Bultreys[1]

[1] Ghent University, Centre for X-Ray Tomography (UGCT), Pore-scale Processes in Geomaterials Research group (PProGRess), Krijgslaan 281/ S8, 9000 Ghent, Belgium, e-mail: Arjen.Mascini@UGent.be

[2] Utrecht University, Dept. of Earth Sciences, Environmental hydrogeology, Princetonlaan 8a, 3584 Utrecht, The Netherlands

Abstract

Capillary-dominated multiphase flow in porous materials is strongly affected by the pore walls' wettability. Recent micro-computed tomography (mCT) studies show that contact angles can be measured inside the pores if the fluid distribution is static. However, this may not be directly relevant to dynamic fluid displacements. Here, we approximate receding contact angles locally in time and space on time-resolved mCT datasets of drainage in a glass bead pack and a limestone. Whenever a fluid meniscus suddenly entered one or more pores, geometric and thermodynamically consistent contact angles in the surrounding pores were measured in the time step just prior to the displacement event. We introduce a new force-based contact angle, defined to recover the measured capillary pressure in the invaded pore throat prior to interface movement. While the static method results in unexpectedly wide contact angle distributions, the new geometric and force-based contact angles followed plausible, narrower distributions and were mutually consistent. We were not able to obtain credible results for the thermodynamically consistent event-based method, likely due to uncertainties in image analysis and neglecting viscous dissipation. Time-resolved mCT analysis can yield a more appropriate wettability characterization for pore scale models, despite the need to further reduce image analysis uncertainties.

Graphical abstract

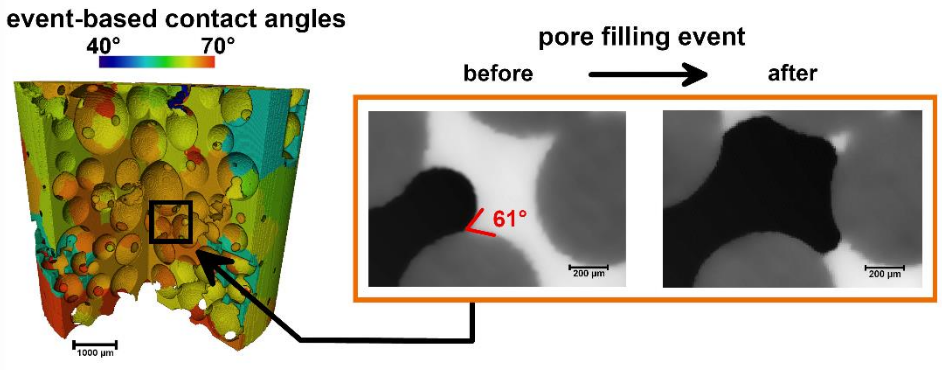

Keywords

Contact angle, Pore-scale, Wettability, Multiphase flow, porous media, imaging, X-ray micro-tomography, interfacial curvature, Haines jump, Primary drainage

1. Introduction

Multiphase flow in porous materials is crucial for e.g. safe subsurface CO_2 storage (Bui et al., 2018), groundwater remediation (Mercer and Cohen, 1990) and efficient PEM fuel cells (Borup et al., 2007; Gostick et al., 2006). This process is strongly affected by the porous medium's wettability: its affinity to be in contact with one fluid over another (Abdallah et al., 2007). The wettability, typically expressed as a contact angle between the solid and the fluids, induces capillary forces which exert a strong influence on fluid displacement (Singh et al., 2019). Drainage is the displacement of a wetting fluid by a non-wetting fluid, while the reverse process is called imbibition (Blunt, 2017). Fundamentally, wettability is a function of the intermolecular forces between the fluids and the solid surface (including any coatings or impurities on it). In addition, most natural materials contain surface roughness from the nanometer scale upwards, which influences the effective contact angle observed at larger scales (Schmatz et al., 2015). Due to local variations in mineralogy, surface roughness and coating, contact angles in porous media are often hysteretic, scale-dependent and variable throughout the pore space (Abdallah et al., 2007; Alhammadi et al., 2017; AlRatrout et al., 2018; Buckley, 2001; Cassie and Baxter, 1944; Khishvand et al., 2016; Morrow, 1990; Murison et al., 2014; Quéré, 2008; Singh et al., 2016; Wenzel, 1936). One of the main open standing questions is therefore how to define and measure local wettability characteristics throughout the pore space with relevance to multiphase fluid dynamics. This is particularly important to inform pore-scale computational models (Akai et al., 2019b; Verma et al., 2018; Zhao et al., 2019).

Recent work has shown that contact angles can be measured by geometrical analysis on a 3D image of fluids in the pore space where the interfaces between the fluids remain static. Such images are typically acquired using micro-computed X-ray tomography (mCT), which has been established as an important tool to investigate multiphase flow at the pore scale in recent years (Andrew et al., 2015; Berg et al., 2013; Blunt, 2017; Bultreys et al., 2016; Wildenschild and Sheppard, 2013). Local measurements of geometrical contact angles in the pore space can be made based on visual observation (Andrew et al., 2015; Khishvand et al., 2017), automated algorithms (AlRatrout et al., 2017; Scanziani et al., 2017) or methods based on the deficit curvature of the solid and fluid interfaces (Sun et al., 2020). However, these measurements were shown to result in unexpectedly wide distributions of contact angles which are difficult to interpret and to use in pore scale models (Akai et al., 2019a; Blunt et al., 2019). This is not fully explained by the significant uncertainty on determining the three-phase contact line and the normal to the rough solid surface, caused by partial volume effects and other imaging artefacts common in mCT (Cnudde and Boone, 2013).

None of the methods discussed so far take into account that contact angles measured on static fluid distributions may not be directly relevant to dynamic fluid displacements during drainage and imbibition. Due to unresolved roughness on the solid surface, contact angles can be hysteretic: at a pinned contact line in any pore, these can vary between an advancing and a receding value, at which the contact line finally starts to move. Furthermore, the location of the contact line in combination with the pore shape at the time of observation, as well as the equilibration time before imaging, likely also influence the observed contact angles (Rabbani et al., 2018; Sun et al., 2020). Such effects cannot be discerned from an image of a fluid distribution at one specific time. Blunt et al. (2019) addressed these concerns by indirectly estimating a thermodynamically consistent contact angle based on energy conservation. They compared mCT images of fluids in a rock sample at the start and end of imbibition, and then equated the pressure-volume work, estimated by measuring the curvature of the fluid-fluid interface and the saturation change, to the interfacial energy stored in the system. The latter can be expressed in function of interfacial areas and a thermodynamically consistent contact angle. The sensitivity to contact line and solid surface normal estimation is therefore reduced or eliminated. Furthermore, this definition aims to take the effects of unresolved solid surface features into account, as it should yield an effective value related to the fluid displacement. Yet, two important issues remain. First, the method assumes that the invasion process can be approximated as being reversible, while this is unlikely to hold for general displacements. (Seth and Morrow, 2007) found that up to 84% of the pressure-volume work during drainage of a limestone was dissipated. Second, the method provides a single contact angle value for the whole sample, rather than a localized measurement.

In this work, we propose to estimate pore-scale (receding) contact angles that are relevant to fluid displacement by analyzing time-resolved mCT datasets. First, we identified the time and location of pores in which fluid displacements took place during drainage. Then, geometric and thermodynamically consistent contact angles were computed on a pore-by-pore basis for each single displacement event at the time just before displacement. We introduce a new force-based receding contact angle definition derived from the measured curvature of a fluid meniscus which triggers it to move through a pore throat (i.e. a Haines jump). The method was tested on two publicly available drainage datasets (Schlüter et al., 2016; Singh et al., 2018).

The methodology and the experimental data are described in Section 2. In section 3.1, the results from the detection of pore filling events are discussed, followed by a validation of the interfacial curvature analysis by experimental capillary pressure data in Section 3.2. In Section 3.3, the novel time-resolved contact angle measurements are compared to the prior static approach and to each other. This is followed by conclusions and discussion of the current limitations of the method in Section 4.

2. Materials and methods

In the following section, the conceptual framework for this study is first introduced, followed by a brief overview of the experimental data and a detailed description of the image analysis workflow used to identify filling events and calculate force-based, geometric and thermodynamically consistent contact angles.

2.1 Contact angles and displacement events

At low capillary numbers, drainage takes place as a sequence of unstable fluid redistribution events (Haines jumps) every few (tens of) seconds, interspersed by smooth reversible displacement (Armstrong and Berg, 2013; Haines, 1930; Morrow, 1970; Schlüter et al., 2017). During the smooth reversible displacement, the contact line can remain (nearly) static close to a local constriction (‘pore throat’) while the curvature of the interface increases due to the increasing capillary pressure (Figure 1), as described by the Young-Laplace equation:

$$P_c = \sigma\left(\frac{1}{R_1} + \frac{1}{R_2}\right) = 2\kappa\sigma \qquad \text{(e.q. 1)}$$

Where σ is the interfacial tension, R_1 and R_2 are the principle radii of curvature of the fluid-fluid interface and κ is its mean curvature.

When the pressure difference between the two fluids exceeds a certain capillary pressure threshold, an irreversible displacement takes place and the interface abruptly enters one or more neighboring pores (local dilations in the pore space). This threshold is determined by the geometry of the pore throat through which the interface has to pass – the narrower the throat, the higher the threshold – as well as by the local wettability. For example, the associated threshold curvature κ_{thr} in a cylindrical pore throat is given by the well-known Young-Laplace equilibrium pressure:

$$P_{c,thr} = 2\sigma\kappa_{thr} = \frac{2\sigma cos(\theta)}{r} \qquad \text{(e.q. 2)}$$

Where θ is the receding contact angle, and r is the throat radius. Therefore, the local wettability in a pore throat can be characterized by defining a force-based receding contact angle θ_f relevant to the displacement:

$$\theta_f \equiv acos(\kappa_{thr} r) \qquad \text{(e.q. 3)}$$

Note that the force-based contact angle only yields the same value as the receding contact angle for perfectly cylindrical pore throats. However, the advantage is that it provides a direct link to the threshold capillary pressure without depending on highly scale-dependent measurements at or near the rough solid interface. Furthermore, e.q. 3 can in principle be extended to arbitrarily complex geometrical pore throat models, e.g. pore throats with triangular (Ma et al., 1996) or hyperbolic polygonal cross-sections (Joekar-Niasar et al., 2010). In this paper, we used the cylindrical model to obtain a first order estimate of the force-based receding contact angle for several hundreds of Haines jumps in a bead pack and a limestone. The following sections describe how θ_f can be estimated for each individual displacement event in time-resolved mCT datasets, as well as how geometrical and thermodynamically consistent contact angles were determined for comparison.

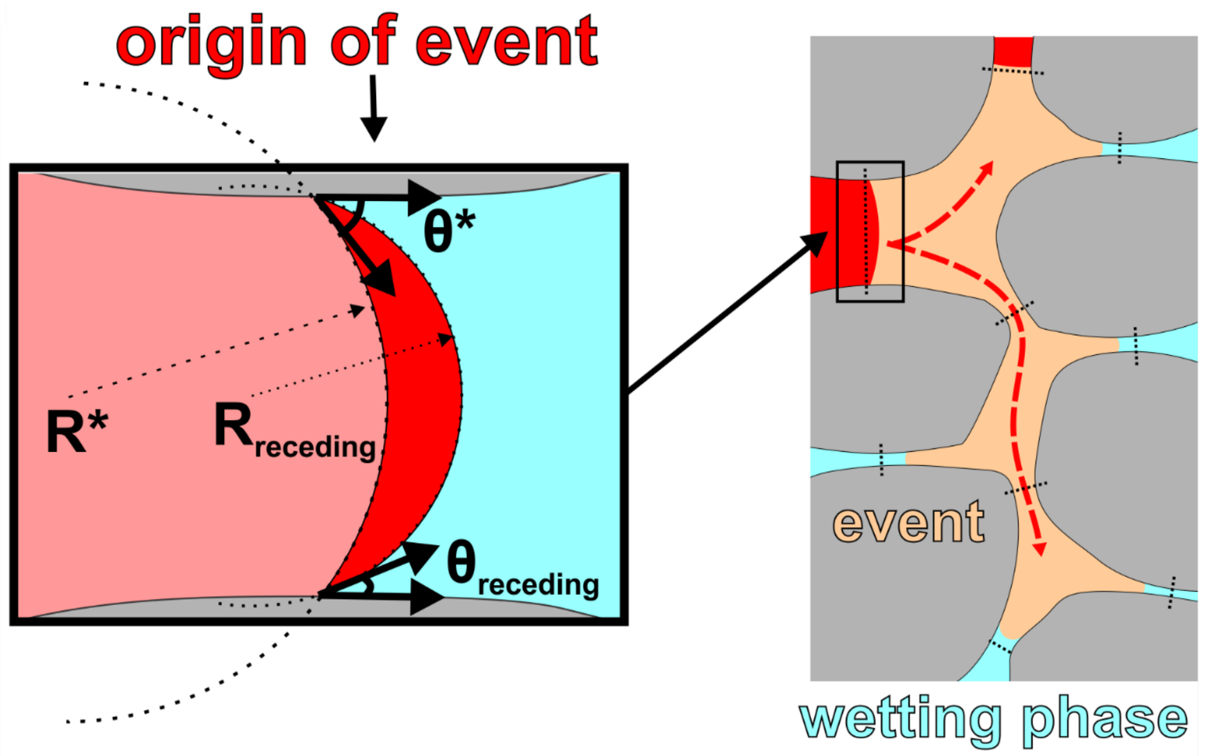

Figure 1 A schematic drawing of a Haines jump during primary drainage. ***Left box:*** *at time T-1 the main terminal meniscus of the non-wetting phase (in pink) is located in a pore throat with an interface with a certain radius of curvature (R^*) and associated contact angle θ^*. Just before displacement (in red), the interface reaches a radius of curvature ($R_{receding}$) and an associated contact angle $\theta_{receding}$ upon which it will start to move into the next pore. $R_{receding}$ determines the threshold capillary pressure for the event.* ***Right box:*** *in the following displacement event, three neighboring pores (indicated in orange and separated by constrictions indicated as black dotted lines) are filled by the Haines jump. Fluid distributions at T-1 are in red and at time T in orange.*

2.2 Experimental data

Two well-documented and publicly available primary drainage data sets were analyzed: one measured on a sintered glass bead pack (Schlüter et al., 2016) and one on a Ketton limestone (Singh et al., 2018). Both experiments are unsteady-state drainage experiments in which a non-wetting phase is injected into a cylindrical sample at a low capillary number to ensure capillary dominated flow. A summary of the experimental parameters is given in Table 1. The time resolved mCT experiments resulted in a series of segmented 3D images, each representing the fluid distribution in the pore space during a discrete, short time interval in the drainage. The data used in our analysis, is the segmented data by Schlüter et al., (2016) and (Singh et al., 2018). The former used a modified form of Markov random field (MRF) segmentation for this, the latter a seeded watershed algorithm.

*Table 1 Overview of the data sets used for the image analysis. * exact flow rates were not recorded during the drainage experiments.*

	glass bead pack	**Ketton limestone**
Sample dimension	5.8mm dia. x 7mm long	3.8mm dia. x 10mm long
Boundary condition	constant flowrate	constant pressure + tight capillary plate
Fluids	n-dodecane, CsCl-brine	n-decane, KI-brine
Interfacial tension	36mN/m	52.33mN/m
Flow rate	50 µl/h	~1-6 µl/h*
Imposed pressure	N/A	50kPa
Capillary number	$4.2*10^{-8}$	$\sim 10^{-9}$*
Number of time steps	38	496
Time per time step	113s	38s
Time span (hr:min:sec)	01:13:44	5:14:08
Reconstructed voxel size	8.4 µm	3.28 µm
Reference	Schlüter et al., (2016)	Singh et al., (2018)

2.3 Image analysis

2.3.1 Identifying fluid filling events in time-resolved mCT datasets

As a first step in the analysis, the pore space was divided into individual pores separated by throat surfaces using a watershed algorithm implemented in the open source algorithm “pnextract” (Raeini et al., 2018) (Figure 2). This algorithm determines the largest inscribed spheres in each pore and in each throat. Pore and throat radii were found as the radii of these inscribed spheres. Following the procedure proposed in Bultreys et al. (2018), 3D images of the determined inscribed spheres in the pores were overlain on the drainage datasets. The fluid occupancy of pore centers was then determined by checking if the majority of the voxels in the associated inscribed sphere were filled with wetting or non-wetting phase. This was done for each pore in each time step, and “fluid filling” was consecutively found as the case where a pore changes its fluid occupancy (i.e. the fluid in the majority of its inscribed sphere’s voxels) in consecutive time steps. Connected fluid fillings in the same time step were regarded to belong to the same filling event (Figure 1). This was done by performing a graph-based connectivity clustering of the pores filled in each time step using MATLAB (Bultreys et al., 2015). Finally, the result of this analysis was a list of filling events, detailing the time of filling, the pores that were filled (including location and characterization of the pores), and the pores and throats that neighbor each filling event. The source throat of each event was found by selecting the throat neighbor with the largest throat radius.

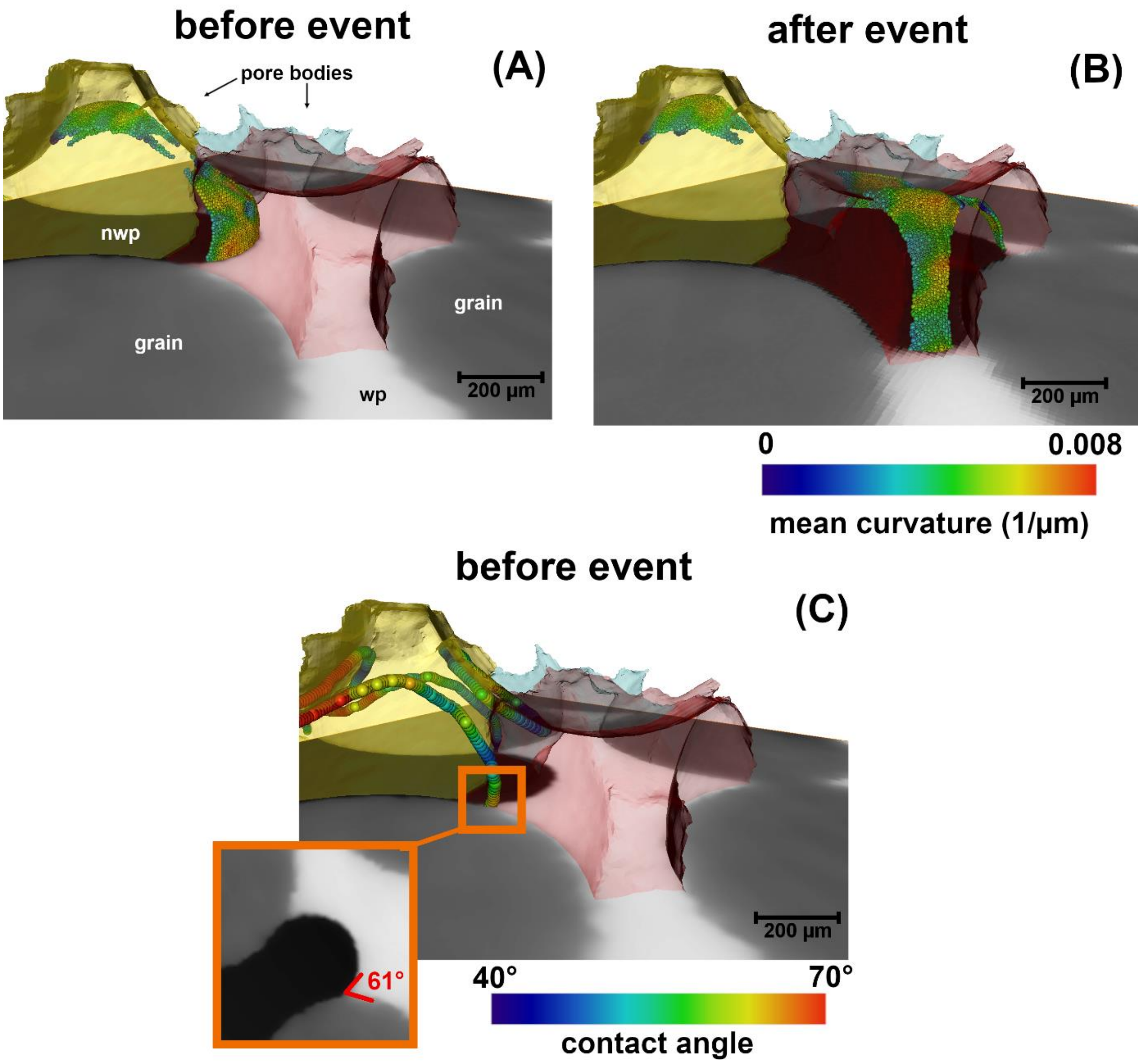

Figure 2 Capturing and characterizing a pore filling event in the sintered glass bead pack dataset from Schlüter et al. (2016). nwp = non-wetting phase, wp = wetting phase. (A) before the event, a non-wetting phase terminal meniscus is located at a pore throat of the yellow pore body. The interface has a mean curvature proportional to the local capillary pressure which is used to determine the force-based contact angle. (B) at the time step after the event, the interface has moved into the neighboring blue and red pore bodies. (C) the event-based geometric contact angle (62°) is calculated by measuring the contact angle on the points of three-phase contact line, indicated by colored spheres. A manual measurement (small box) of the contact angle in the plane perpendicular to the grain surface is in reasonable agreement (61°) with the event-based geometric contact angle.

2.3.2 Force-based receding contact angles

As defined in section 2.1, an estimate for the force-based contact angle can be obtained by linking the local capillary pressure which triggered the fluid redistribution to the radius of the source throat of each event. On 3D images of fluid distributions, the local capillary pressure can be estimated from the curvature of the fluid–fluid interface (Andrew et al., 2014a; Armstrong et al., 2012). As the volume in space associated to each pore is known, it is straightforward to map point measurements of interfacial curvature to pores. At time step T-1, before a filling event, the fluid-fluid interface is located (partly) in the pores directly neighboring the event. Therefore, we determined the average fluid-fluid interfacial curvature both in pores that were invaded and in their neighbors during the time-step just before the associated filling event (Figure *2*A).

To obtain curvature values, the fluid-fluid interface was extracted from the segmented images by extracting a triangulated surface using the marching cube algorithm (Lorensen and Cline, 1987) in Avizo (ThermoFisher Scientific). Constrained surface smoothing using a Gaussian filter with an extent of 3 voxels was performed, analogous to Li et al. (2018). Mean surface curvature was calculated using the eigenvalues and eigenvectors of a quadratic form fitted locally to the surface. The accuracy of this calculation is limited by the finite resolution of the images, especially in regions close to the three-phase contact line, where partial volume effects add to the uncertainty, and in arc-meniscus sections of the fluid-fluid interface (Akai et al., 2019b; Armstrong et al., 2012; Li et al., 2018; Singh et al., 2017). The curvature data points were filtered based on several criteria to account for this. First, all data points with a curvature corresponding to a radius of curvature smaller than twice the reconstructed voxel size were omitted as these most likely represent noise. The non-wetting phase bulges into the wetting phase during drainage and terminal menisci thus have a positive curvature with respect to the non-wetting phase (Armstrong et al., 2012). As this study is limited to drainage, all data points with a curvature equal to or smaller than zero, typically associated with arc-meniscus sections of the interface, were subsequently filtered out. Lastly, we followed the approach of Li et al. (2018) on the glass bead data set, to filter and weigh the curvature data points based (AlRatrout et al., 2017; Blunt et al., 2019; Dalton et al., 2018) on their geodesic distance (20% of the maximum geodesic distance found in the image) to the edge of the surface. For the Ketton data set, we followed the approach of Singh et al. (2017) by filtering data points with a Euclidian distance of 3 voxels from the pore wall.

2.3.3 Geometric (receding) contact angles

To reduce uncertainty related to the state of the interface (e.g. pinning), receding contact angles have to be measured at (or at least very near) the moment the fluid-fluid interface moves. Therefore, we propose to measure geometric contact angles at the appropriate time step in a small region directly surrounding the displacement event in time-resolved mCT data. This is in contrast to previous measurements of geometric contact angles that included all points on the three phase contact lines in a single mCT image of a static fluid distribution, typically acquired at the end of drainage or imbibition (e.g. AlRatrout et al., 2017; Blunt et al., 2019; Dalton et al., 2018).

We compared both approaches of contact angle measurements using the fully automatic algorithm developed by AlRatrout et al. (2017). The algorithm generated a smoothed mesh on which the three phase contact line is identified. Subsequently, it calculated geometric contact angles in each mesh point on the contact line based on the dot product of the vectors normal to the solid surface and the fluid-fluid interface. We used the default smoothing settings proposed by AlRatrout et al. (2017). The method was applied to each time step image. Event-based geometric contact angles were then determined by retaining and averaging only the geometric contact angle points measured in the event pores and their neighbors at the appropriate event time step (Figure 2C). We compared this to the conventional static method by calculating the distribution of all the contact angle points in the last time step of drainage.

2.3.4 Thermodynamically-consistent receding contact angles

Here, we extend the work of Morrow (1970) and Blunt et al. (2019) to derive a thermodynamically-consistent contact angle, θ_t, for filling events during primary drainage:

$$cos\theta_t = \frac{\kappa_{thr}\Delta V_{nwp}+\Delta A_{fluid-fluid}}{\Delta A_{nwp-solid}} \quad \text{(e.q. 4)}$$

Where κ_{thr} is the threshold curvature at invasion, ΔV_{nwp} the change in volume of the non-wetting phase (positive for primary drainage), $\Delta A_{fluid-fluid}$ the change in fluid-fluid interfacial area, and $\Delta A_{nwp-solid}$ the change in non-wetting-solid surface area (positive for primary drainage). Surface areas were calculated on triangulated surfaces extracted using the method described in Section 2.3.2. By applying this relationship, drainage is assumed to be an isothermal, reversible process, which has been shown not to be valid in general (Armstrong and Berg, 2013; Morrow, 1970; Seth and Morrow, 2007). The calculated thermodynamically-consistent contact angle is therefore likely an underestimation, as part of the work done will be lost as viscous dissipation (Blunt et al., 2019). Similar to the calculation of the geometric receding contact angle, we compare the event-by-event based results to a static calculation using surface areas, curvatures and volumes of consecutive time step images.

3. Results & discussion

3.1 Filling events

By detecting changes in pore occupancy during the experiments and clustering these into pore filling events (section 2), 231 (glass bead pack) and 425 (Ketton limestone) filling events were detected and analyzed. Up to 17 (glass beads) and 8 (Ketton limestone) different events were detected in a single time step (Figure 3). The number of pore-filling events per time step increases over time (Figure 3) while the volumes of these events decreases (Figure 4). Well connected, larger pores were filled first, and smaller pores with fewer connections were filled later in the sequence, as expected from invasion percolation.

Table 2 Overview of the detected events in the glass bead pack and Ketton limestone

	glass bead pack	**Ketton limestone**
Events	231	425
multi-pore events	95	134
Large events (>1% pore volume, #pores)	20	4
Largest event (# pores)	18	46

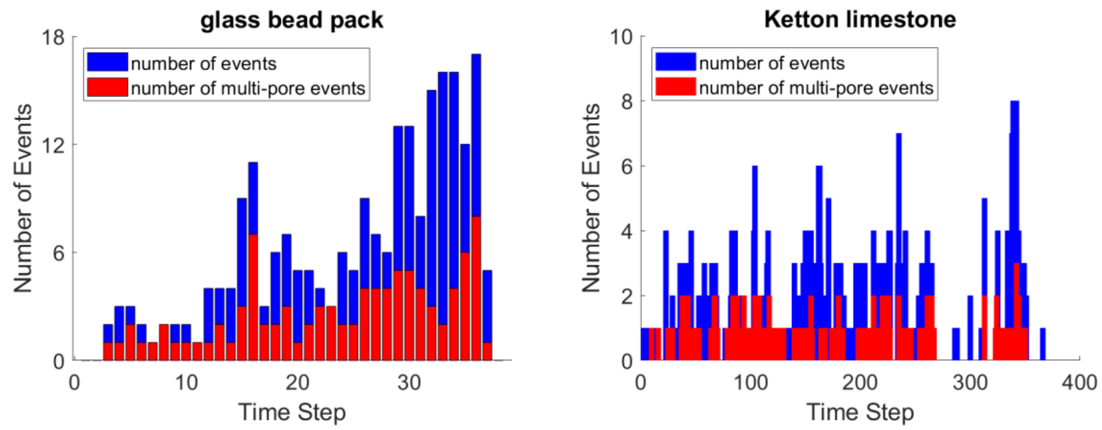

Figure 3 Bar charts showing the number of (multi-pore) events detected per time step.

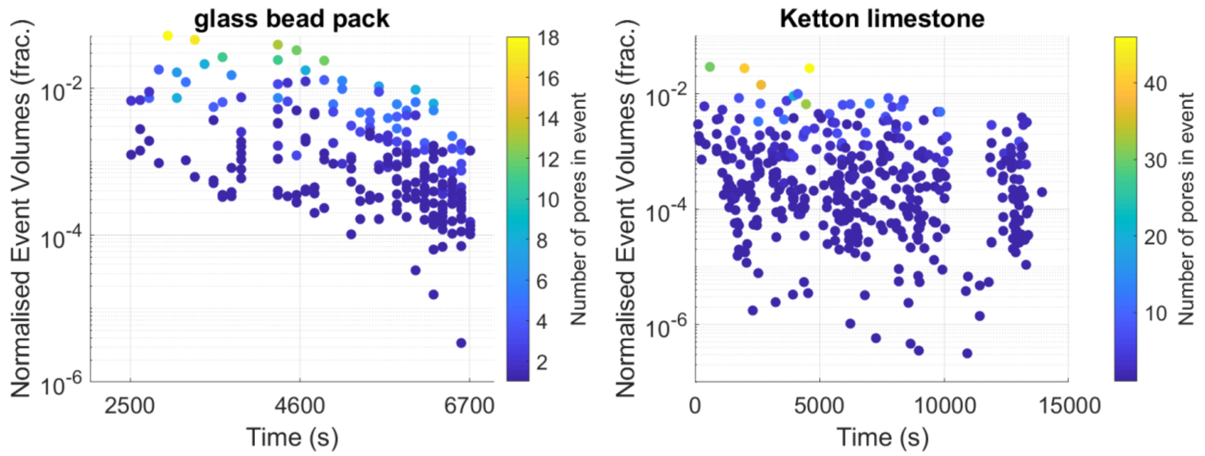

Figure 4 Plots showing the normalized event volume for each event with the number of pores filled during the event in colors.

<u>3.2 Validation of curvature measurements</u>

The force-based contact angle introduced in this paper depends crucially on the measurement of interfacial curvature from the time-resolved mCT scans. Using e.q. 1, these measurements also yield the associated capillary pressure, which can be plotted against the wetting saturation determined from the image (Figure 5). The resulting threshold capillary pressures can thus be compared and validated to capillary pressure curves measured with external pressure transducers (Armstrong et al., 2012). Experimental pressure measurements were available for the glass bead pack dataset, but not for the Ketton limestone dataset. We validated the latter using mercury intrusion capillary pressure (MICP) data, measured on a different Ketton limestone sample (Reynolds and Krevor, 2015). We rescaled the saturation axis of the MICP data to include only the pore space larger than the voxel size of the images (3.28µm). The Pc axis was rescaled using the interfacial tension measured by (Singh et al., 2018) and a range of contact angle values (20°-60°) expected for Ketton limestone.

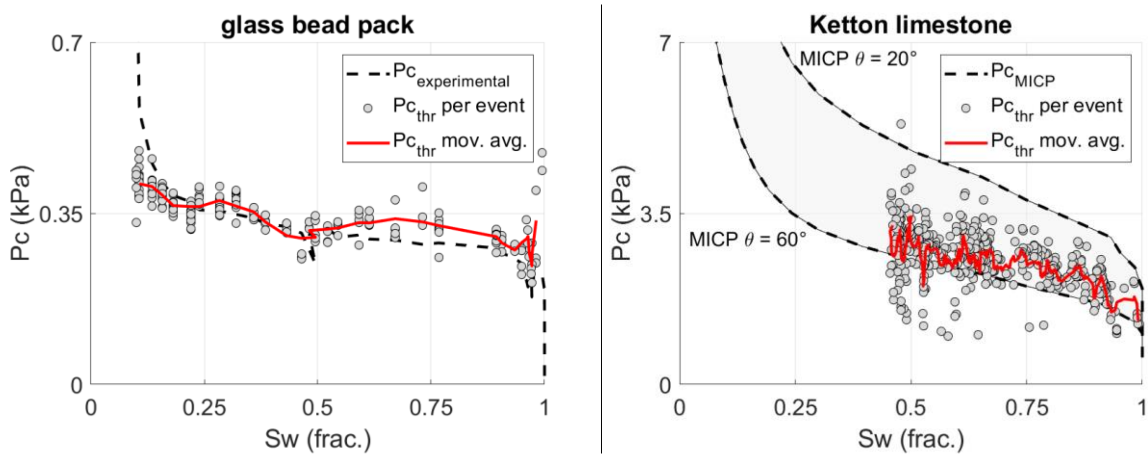

Figure 5 Calculated threshold capillary pressure for each event plotted against the wetting-phase saturation of the sample calculated from the images. The data is compared to experimental pressure measurements in the case of the glass bead pack and scaled MICP measurements (Reynolds and Krevor 2015) using a theta between 20° and 60° for the data of the Ketton limestone.

As can be seen in Figure 5, the event-based calculations scatter around the externally measured pressures. The scatter is to some extent expected for drainage, since non-local effects can induce local pressure differences and the time scale of the experiments is likely too short to establish full capillary equilibrium (Armstrong and Berg, 2013; Schlüter et al., 2017).

Imaging and image analysis form additional sources of uncertainty. Limited spatial resolution causes uncertainty in the calculated mean curvature of the interface as the curvature is not fully resolved. Akai et al. (2019) estimated that local capillary pressures can be estimated within 30% if the average radius of curvature is more than 6 times the image resolution. Applying these rules of thumb, a radius of curvature of 6 times the image resolution would be equivalent to capillary pressures of ~0.7 kPa and ~2.6 kPa for the glass beads and Ketton limestone respectively. As these values are close to the measured pressures, the spatial resolution is likely to influence the results, especially at lower wetting phase saturations. The limited temporal resolution of the scans causes motion artefacts and decreases the signal to noise ratio, providing additional sources of uncertainty. Furthermore, this also means that the curvature is determined a few tens of seconds before the Haines jump. To estimate the uncertainty induced by this, we determined the average rate of change of the external Pc measurement in the glass bead pack. This was ~43 Pa per time step, equating to an uncertainty of approximately 10% on the average measured event pressures. However, the uncertainty is less significant in the beginning of drainage, and more significant at the very end (when the Pc is changing more rapidly). The temporal uncertainty on the Ketton dataset can be assumed to be lower, as both the flow rate and the time per image are smaller (Table 1), yet there are no external pressure measurements available to estimate this quantitatively. Newer synchrotron beamline setups allow to further increase the temporal resolution by 2 orders of magnitude (1s/scan) without compromising the image quality (Mokso et al., 2017; Spurin et al., 2019).

3.3 Force-based, geometric and thermodynamically consistent contact angles

The distribution of the force-based contact angles is compared to those of the static and event-based geometric contact angles and of the event-based thermodynamically consistent contact angles in Figure 6. The average force-based contact angle was 63° and 56° in respectively the glass bead pack and the Ketton limestone datasets, compared to an average event-based geometric contact angle of respectively 64° and 57°. The distribution of the event-based geometric contact angles matched the force-based angle closely. The event-based geometric contact angle has a notably narrower distribution than its "static" counterpart (the distribution of all geometric contact angles measured in one time step image). This confirms that the unexpectedly wide contact angle distributions reported in literature are to a significant extent related to the dynamics of the interface motion, e.g. contact angle hysteresis, pinning, the location of the contact line at the time of fluid redistribution, or interface relaxation. The event-based thermodynamically consistent contact angles are more broadly distributed than the geometric and force-based methods. They had a lower mean value than the other methods for the glass beads (48°) and a higher value for Ketton limestone (66°). Similar values, 44° and 68° for the glass bead pack and Ketton limestone respectively, were found when using the approach of Blunt et al. (2019), using the full fluid distributions on consecutive images for the calculations.

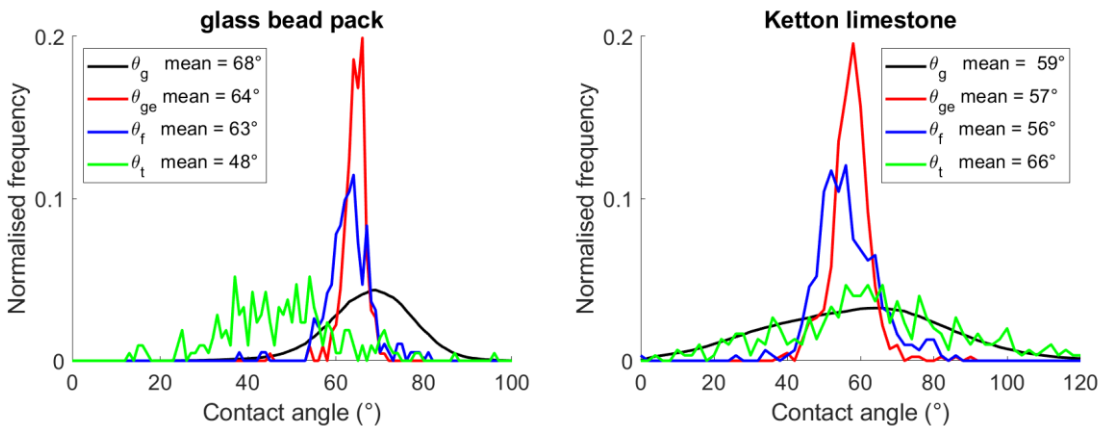

Figure 6 Distribution of force-based (θ_f), geometric (θ_{ge}) and thermodynamically consistent (θ_t) contact angles determined on an event-by-event basis using the proposed methodology, compared to the standard approach of determining the geometric contact angles in each point on the contact line of the mCT image taken after drainage (θ_g).

The contact angle values for each event are cross-plotted in Figure 7. The fairly good match between the force-based and the geometric methods suggests that geometric contact angles can be used to provide a reasonable prediction of the invasion capillary pressure in pore scale drainage models, yet only when measured on an event-by-event basis in a time-resolved dataset. This is crucial for e.g. pore network modelling studies, which predict the drainage filling sequence by sequentially invading pores in order of increasing threshold capillary pressure (invasion percolation). However, it is also clear that there was still a significant amount of scatter in the data, related to the spatial and temporal resolutions on the one hand and the irregular shape of the throats in realistic porous materials on the other hand. The latter could be improved by refining the definition of the force-based contact angle (e.q. 2). Both sources of uncertainty are consistent with higher scatter in Ketton than in the simpler, wider pore space of the glass bead pack. The calculated thermodynamically consistent contact angles show significantly more scattering than the force-based contact angles (Figure 7). In addition, the equation yielded imaginary values for the contact angle for 17 events in the glass bead pack data set and 125 in the Ketton limestone data set. The increased scatter could be attributed to both the added uncertainty in the calculations of fluid-fluid and fluid-solid surface areas and the assumption of no viscous dissipation.

Intuitively, receding contact angles in smooth, water-wet media are expected to be lower than the reported values. Manual observations using the method described by Andrew et al. (2014b) confirmed contact angles around 50° - 60° (e.g. Figure 2) in both the glass beads and Ketton limestone data set, showing that these were likely not induced by the automatic image analysis method. As shown in Figure 7, the calculated values were consistent with a description of the fluid displacement at the scale of observation, and can thus be used directly for pore scale modelling. The discrepancy may be due to the converging geometry of pore throats, which was shown to increase the “effective” contact angle (i.e. the one linked to the fluid-fluid interfacial curvature) (Rabbani et al., 2018). Finally, it should also be noted that the limited temporal resolution of the mCT data tended to yield an underestimation of the fluid-fluid curvature, as the capillary pressure rises continuously during image acquisition, resulting in a slight overestimation of the contact angles.

As shown in Figure 8, the values of event-based contact angles can be mapped back to the original pore space. This spatial data could be used to improve numerical simulations of multiphase flow by incorporating local information on the wettability of the sample, which could be especially valuable for samples with a mixed-wettability.

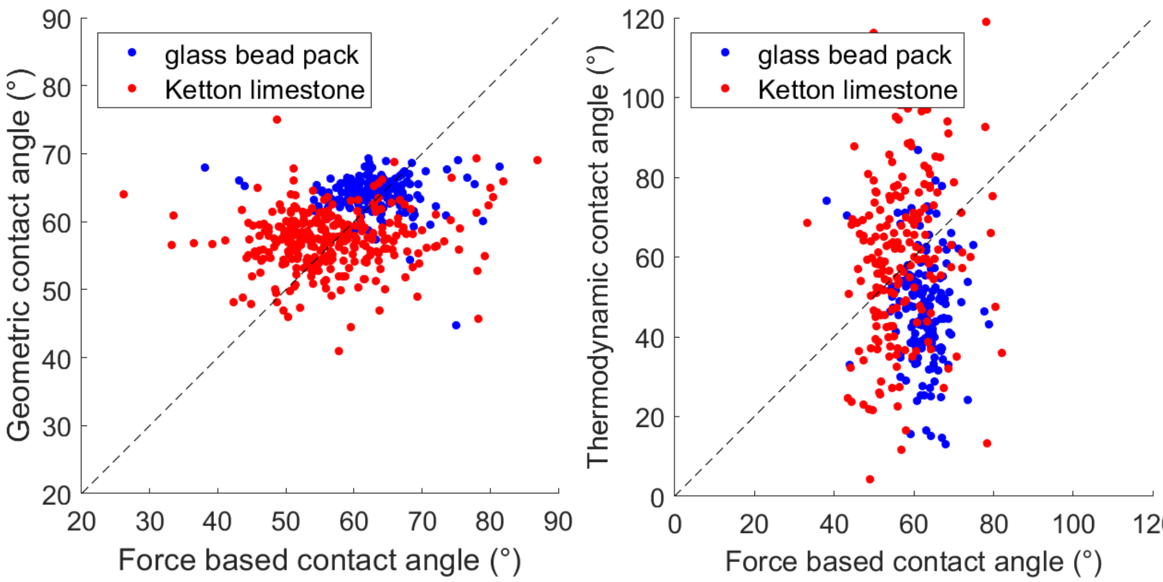

Figure 7 Left: the geometric versus the force-based contact angle for individual events detected in the two drainage datasets. Right: the thermodynamically consistent versus the force-based contact angle for individual events in the two drainage datasets.

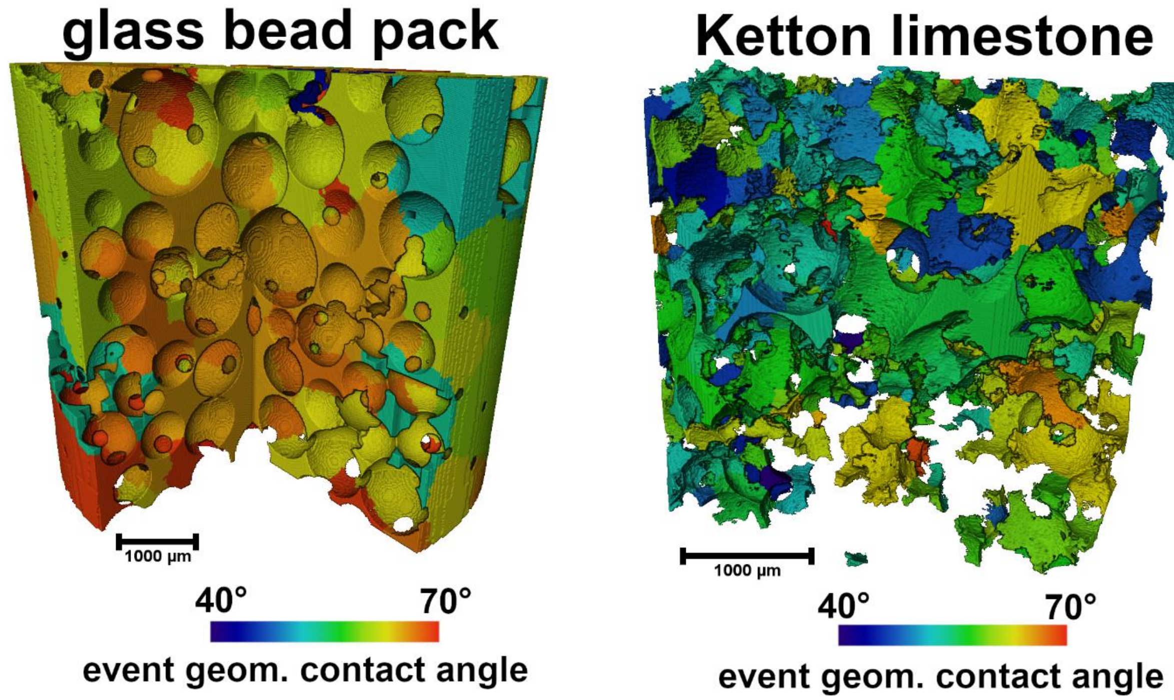

Figure 8 Rendering of the 3D distribution of the event-based geometric contact angle for each pore.

4. Conclusion and outlook

This work aims to improve our understanding of wettability by calculating receding contact angles for individual pore-filling events, rather than for a static fluid distribution as a whole. The proposed method was applied to two unsteady state drainage data sets: a sintered glass bead pack and a Ketton limestone. Event-based geometric contact angles show a distinctively narrower distribution than when these are calculated on the entire static fluid distributions (e.g. AlRatrout et al., 2017; Blunt et al., 2019; Dalton et al., 2018), suggesting that wide contact angle distributions are likely caused by the unaccounted for dynamics of the interface. We introduce a force-based contact angle, which shows that event-based geometric contact angles produce plausible threshold capillary pressures for associated pore filling events. This suggest that event-based geometric contact angles may provide valid effective contact angles for the displacement process and are more appropriate for use in pore scale modeling. Despite these promising first results, we note the need for enhanced image quality and image processing methodologies to reduce the uncertainty of the proposed methods. Due to these uncertainties, we were not able to draw conclusions on the appropriateness of the thermodynamic contact angle as a concept.

Future work should point out if the described method can be used to quantify wettability for mixed-wettability systems and during imbibition. The success hereof would benefit of the increased temporal and spatial resolution available at synchrotron facilities optimized for fast imaging (Mokso et al., 2017) and advances in iterative reconstruction techniques developed for low signal to noise ratios (Chen et al., 2008; Myers et al., 2011). This enhanced image quality is crucial to distinguish different displacement mechanism during imbibition and to improve the accuracy in calculating interfacial curvature and area.

Acknowledgements

Dr. Steffen Schlüter and Dr. Kamaljit Singh are thanked for making their data available and their helpful discussions. This research received funding from the Research Foundation–Flanders (FWO, project G051418N). Tom Bultreys is a postdoctoral fellow of the Research Foundation–Flanders (FWO) and acknowledges its support under grant 12X0919N. The data used in this manuscript is freely available online, as cited in the main text.

References

Abdallah, W., Buckley, J.S., Carnegie, A., Edwards, J., Herold, B., Fordham, E., Graue, A., Habashy, T., Seleznev, N., Signer, C., Hussain, H., Montaron, B., Ziauddin, M., 2007. Fundamentals of Wettability. Oilfield Review 18.

Akai, T., Alhammadi, A.M., Blunt, M.J., Bijeljic, B., 2019a. Modeling Oil Recovery in Mixed-Wet Rocks: Pore-Scale Comparison Between Experiment and Simulation. Transport in Porous Media 127, 393–414. https://doi.org/10.1007/s11242-018-1198-8

Akai, T., Lin, Q., Alhosani, A., Bijeljic, B., Blunt, M., 2019b. Quantification of Uncertainty and Best Practice in Computing Interfacial Curvature from Complex Pore Space Images. Materials 12, 2138. https://doi.org/10.3390/ma12132138

Alhammadi, A.M., AlRatrout, A., Singh, K., Bijeljic, B., Blunt, M.J., 2017. In situ characterization of mixed-wettability in a reservoir rock at subsurface conditions. Scientific Reports 7. https://doi.org/10.1038/s41598-017-10992-w

AlRatrout, A., Blunt, M.J., Bijeljic, B., 2018. Wettability in complex porous materials, the mixed-wet state, and its relationship to surface roughness. Proceedings of the National Academy of Sciences 201803734. https://doi.org/10.1073/pnas.1803734115

AlRatrout, A., Raeini, A.Q., Bijeljic, B., Blunt, M.J., 2017. Automatic measurement of contact angle in pore-space images. Advances in Water Resources 109, 158–169. https://doi.org/10.1016/j.advwatres.2017.07.018

Andrew, M., Bijeljic, B., Blunt, M.J., 2014a. Pore-by-pore capillary pressure measurements using X-ray microtomography at reservoir conditions: Curvature, snap-off, and remobilization of residual CO_2. Water Resources Research 50, 8760–8774. https://doi.org/10.1002/2014WR015970

Andrew, M., Bijeljic, B., Blunt, M.J., 2014b. Pore-scale contact angle measurements at reservoir conditions using X-ray microtomography. Advances in Water Resources 68, 24–31. https://doi.org/10.1016/j.advwatres.2014.02.014

Andrew, M., Menke, H., Blunt, M.J., Bijeljic, B., 2015. The Imaging of Dynamic Multiphase Fluid Flow Using Synchrotron-Based X-ray Microtomography at Reservoir Conditions. Transport in Porous Media 110, 1–24. https://doi.org/10.1007/s11242-015-0553-2

Armstrong, R.T., Berg, S., 2013. Interfacial velocities and capillary pressure gradients during Haines jumps. Physical Review E 88, 043010.

Armstrong, R.T., Porter, M.L., Wildenschild, D., 2012. Linking pore-scale interfacial curvature to column-scale capillary pressure. Advances in Water Resources 46, 55–62. https://doi.org/10.1016/j.advwatres.2012.05.009

Berg, S., Ott, H., Klapp, S.A., Schwing, A., Neiteler, R., Brussee, N., Makurat, A., Leu, L., Enzmann, F., Schwarz, J.-O., Kersten, M., Irvine, S., Stampanoni, M., 2013. Real-time 3D imaging of Haines jumps in porous media flow. Proceedings of the National Academy of Sciences 110, 3755–3759. https://doi.org/10.1073/pnas.1221373110

Blunt, M.J., 2017. Multiphase Flow in Permeable Media: A Pore-Scale Perspective. Cambridge University Press.

Blunt, M.J., Lin, Q., Akai, T., Bijeljic, B., 2019. A thermodynamically consistent characterization of wettability in porous media using high-resolution imaging. Journal of Colloid and Interface Science 552, 59–65. https://doi.org/10.1016/j.jcis.2019.05.026

Borup, R., Meyers, J., Pivovar, B., Kim, Y.S., Mukundan, R., Garland, N., Myers, D., Wilson, M., Garzon, F., Wood, D., Zelenay, P., More, K., Stroh, K., Zawodzinski, T., Boncella, J., McGrath, J.E., Inaba, M., Miyatake, K., Hori, M., Ota, K., Ogumi, Z., Miyata, S., Nishikata, A., Siroma, Z., Uchimoto, Y., Yasuda, K., Kimijima, K., Iwashita, N., 2007. Scientific Aspects of Polymer Electrolyte Fuel Cell Durability and Degradation. Chemical Reviews 107, 3904–3951. https://doi.org/10.1021/cr050182l

Buckley, J.S., 2001. Effective wettability of minerals exposed to crude oil. Current Opinion in Colloid & Interface Science 6, 191–196. https://doi.org/10.1016/S1359-0294(01)00083-8

Bui, M., Adjiman, C.S., Bardow, A., Anthony, E.J., Boston, A., Brown, S., Fennell, P.S., Fuss, S., Galindo, A., Hackett, L.A., Hallett, J.P., Herzog, H.J., Jackson, G., Kemper, J., Krevor, S., Maitland, G.C., Matuszewski, M., Metcalfe, I.S., Petit, C., Puxty, G., Reimer, J., Reiner, D.M., Rubin, E.S., Scott, S.A., Shah, N., Smit, B., Trusler, J.P.M., Webley, P., Wilcox, J., Mac Dowell, N., 2018. Carbon capture and storage (CCS): the way forward. Energy & Environmental Science 11, 1062–1176. https://doi.org/10.1039/C7EE02342A

Bultreys, T., Boone, M.A., Boone, M.N., De Schryver, T., Masschaele, B., Van Loo, D., Van Hoorebeke, L., Cnudde, V., 2015. Real-time visualization of Haines jumps in sandstone with laboratory-based microcomputed tomography. Water Resources Research 51, 8668–8676. https://doi.org/10.1002/2015WR017502

Bultreys, T., De Boever, W., Cnudde, V., 2016. Imaging and image-based fluid transport modeling at the pore scale in geological materials: A practical introduction to the current state-of-the-art. Earth-Science Reviews 155, 93–128. https://doi.org/10.1016/j.earscirev.2016.02.001

Bultreys, T., Lin, Q., Gao, Y., Raeini, A.Q., AlRatrout, A., Bijeljic, B., Blunt, M.J., 2018. Validation of model predictions of pore-scale fluid distributions during two-phase flow. Physical Review E 97. https://doi.org/10.1103/PhysRevE.97.053104

Cassie, A.B.D., Baxter, S., 1944. Wettability of porous surfaces. Transactions of the Faraday Society 40, 546. https://doi.org/10.1039/tf9444000546

Chen, G.-H., Tang, J., Leng, S., 2008. Prior image constrained compressed sensing (PICCS): a method to accurately reconstruct dynamic CT images from highly undersampled projection data sets. Medical physics 35, 660–663.

Cnudde, V., Boone, M.N., 2013. High-resolution X-ray computed tomography in geosciences: A review of the current technology and applications. Earth-Science Reviews 123, 1–17. https://doi.org/10.1016/j.earscirev.2013.04.003

Dalton, L.E., Klise, K.A., Fuchs, S., Crandall, D., Goodman, A., 2018. Methods to measure contact angles in scCO2-brine-sandstone systems. Advances in Water Resources 122, 278–290. https://doi.org/10.1016/j.advwatres.2018.10.020

Gostick, J.T., Fowler, M.W., Ioannidis, M.A., Pritzker, M.D., Volfkovich, Y.M., Sakars, A., 2006. Capillary pressure and hydrophilic porosity in gas diffusion layers for polymer electrolyte fuel cells. Journal of Power Sources 156, 375–387. https://doi.org/10.1016/j.jpowsour.2005.05.086

Haines, W.B., 1930. Studies in the physical properties of soil. V. The hysteresis effect in capillary properties, and the modes of moisture distribution associated therewith. The Journal of Agricultural Science 20, 97–116.

Joekar-Niasar, V., Prodanović, M., Wildenschild, D., Hassanizadeh, S.M., 2010. Network model investigation of interfacial area, capillary pressure and saturation relationships in granular porous media: NEW NETWORK MODEL FOR CAPILLARY FLOW. Water Resources Research 46. https://doi.org/10.1029/2009WR008585

Khishvand, M., Alizadeh, A.H., Oraki Kohshour, I., Piri, M., Prasad, R.S., 2017. In situ characterization of wettability alteration and displacement mechanisms governing recovery enhancement due to low-salinity waterflooding: PHYSICS OF LOW-SALINITY WATERFLOODING. Water Resources Research 53, 4427–4443. https://doi.org/10.1002/2016WR020191

Khishvand, M., Alizadeh, A.H., Piri, M., 2016. In-situ characterization of wettability and pore-scale displacements during two- and three-phase flow in natural porous media. Advances in Water Resources 97, 279–298. https://doi.org/10.1016/j.advwatres.2016.10.009

Li, T., Schlüter, S., Dragila, M.I., Wildenschild, D., 2018. An improved method for estimating capillary pressure from 3D microtomography images and its application to the study of disconnected nonwetting phase. Advances in Water Resources 114, 249–260. https://doi.org/10.1016/j.advwatres.2018.02.012

Lorensen, W.E., Cline, H.E., 1987. Marching cubes: A high resolution 3D surface construction algorithm, in: ACM Siggraph Computer Graphics. ACM, pp. 163–169.

Ma, S., Mason, G., Morrow, N.R., 1996. Effect of contact angle on drainage and imbibition in regular polygonal tubes. Colloids and Surfaces A: Physicochemical and Engineering Aspects 117, 273–291. https://doi.org/10.1016/0927-7757(96)03702-8

Mercer, J.W., Cohen, R.M., 1990. A review of immiscible fluids in the subsurface: Properties, models, characterization and remediation. Journal of Contaminant Hydrology 6, 107–163. https://doi.org/10.1016/0169-7722(90)90043-G

Mokso, R., Schlepütz, C.M., Theidel, G., Billich, H., Schmid, E., Celcer, T., Mikuljan, G., Sala, L., Marone, F., Schlumpf, N., others, 2017. GigaFRoST: the gigabit fast readout system for tomography. Journal of synchrotron radiation 24, 1250–1259.

Morrow, N.R., 1990. Wettability and Its Effect on Oil Recovery. Journal of petroleum technology 42, 1–476.

Morrow, N.R., 1970. Physics and Thermodynamics of Capillary Action in Porous Media. Ind. Eng. Chem. 62, 32–56. https://doi.org/10.1021/ie50726a006

Murison, J., Semin, B., Baret, J.-C., Herminghaus, S., Schröter, M., Brinkmann, M., 2014. Wetting Heterogeneities in Porous Media Control Flow Dissipation. Physical Review Applied 2. https://doi.org/10.1103/PhysRevApplied.2.034002

Myers, G.R., Kingston, A.M., Varslot, T.K., Turner, M.L., Sheppard, A.P., 2011. Dynamic tomography with a priori information. Applied optics 50, 3685–3690.

Quéré, D., 2008. Wetting and Roughness. Annual Review of Materials Research 38, 71–99. https://doi.org/10.1146/annurev.matsci.38.060407.132434

Rabbani, H.S., Zhao, B., Juanes, R., Shokri, N., 2018. Pore geometry control of apparent wetting in porous media. Scientific Reports 8. https://doi.org/10.1038/s41598-018-34146-8

Raeini, A.Q., Bijeljic, B., Blunt, M.J., 2018. Generalized network modeling of capillary-dominated two-phase flow. Physical Review E 97. https://doi.org/10.1103/PhysRevE.97.023308

Reynolds, C.A., Krevor, S., 2015. Characterizing flow behavior for gas injection: Relative permeability of CO_2 -brine and N_2 -water in heterogeneous rocks: CHARACTERIZING FLOW BEHAVIOR FOR GAS INJECTION. Water Resources Research 51, 9464–9489. https://doi.org/10.1002/2015WR018046

Scanziani, A., Singh, K., Blunt, M.J., Guadagnini, A., 2017. Automatic method for estimation of in situ effective contact angle from X-ray micro tomography images of two-phase flow in porous media. Journal of Colloid and Interface Science 496, 51–59. https://doi.org/10.1016/j.jcis.2017.02.005

Schlüter, S., Berg, S., Li, T., Vogel, H.-J., Wildenschild, D., 2017. Time scales of relaxation dynamics during transient conditions in two-phase flow: RELAXATION DYNAMICS. Water Resources Research 53, 4709–4724. https://doi.org/10.1002/2016WR019815

Schlüter, S., Berg, S., Rücker, M., Armstrong, R.T., Vogel, H.-J., Hilfer, R., Wildenschild, D., 2016. Pore-scale displacement mechanisms as a source of hysteresis for two-phase flow in porous media. Water Resources Research 52, 2194–2205. https://doi.org/10.1002/2015WR018254

Schmatz, J., Urai, J.L., Berg, S., Ott, H., 2015. Nanoscale imaging of pore-scale fluid-fluid-solid contacts in sandstone: Imaging Fluid-Fluid-Solid Contacts. Geophysical Research Letters 42, 2189–2195. https://doi.org/10.1002/2015GL063354

Seth, S., Morrow, N.R., 2007. Efficiency of the Conversion of Work of Drainage to Surface Energy for Sandstone and Carbonate. SPE Reservoir Evaluation & Engineering 10, 338–347. https://doi.org/10.2118/102490-PA

Singh, K., Bijeljic, B., Blunt, M.J., 2016. Imaging of oil layers, curvature and contact angle in a mixed-wet and a water-wet carbonate rock. Water Resources Research 52, 1716–1728. https://doi.org/10.1002/2015WR018072

Singh, K., Jung, M., Brinkmann, M., Seemann, R., 2019. Capillary-Dominated Fluid Displacement in Porous Media. Annual Review of Fluid Mechanics 51, 429–449. https://doi.org/10.1146/annurev-fluid-010518-040342

Singh, K., Menke, H., Andrew, M., Lin, Q., Rau, C., Blunt, M.J., Bijeljic, B., 2017. Dynamics of snap-off and pore-filling events during two-phase fluid flow in permeable media. Scientific Reports 7. https://doi.org/10.1038/s41598-017-05204-4

Singh, K., Menke, H., Andrew, M., Rau, C., Bijeljic, B., Blunt, M.J., 2018. Time-resolved synchrotron X-ray micro-tomography datasets of drainage and imbibition in carbonate rocks. Scientific Data 5. https://doi.org/10.1038/sdata.2018.265

Spurin, C., Krevor, S.C., Blunt, M.J., Berg, S., Bijeljic, B., Bultreys, T., Rücker, M., Garfi, G., Scanziani, A., Schlepütz, C.M., others, 2019. Imaging of Steady-State Intermittent Flow Pathways in a Carbonate Rock with 1 Second Time Resolution, in: AGU Fall Meeting 2019. AGU.

Sun, C., McClure, J.E., Mostaghimi, P., Herring, A.L., Shabaninejad, M., Berg, S., Armstrong, R.T., 2020. Linking continuum-scale state of wetting to pore-scale contact angles in porous media. Journal of Colloid and Interface Science 561, 173–180. https://doi.org/10.1016/j.jcis.2019.11.105

Verma, R., Icardi, M., Prodanović, M., 2018. Effect of wettability on two-phase quasi-static displacement: Validation of two pore scale modeling approaches. Journal of Contaminant Hydrology 212, 115–133. https://doi.org/10.1016/j.jconhyd.2018.01.002

Wenzel, R.N., 1936. RESISTANCE OF SOLID SURFACES TO WETTING BY WATER. Industrial & Engineering Chemistry 28, 988–994. https://doi.org/10.1021/ie50320a024

Wildenschild, D., Sheppard, A.P., 2013. X-ray imaging and analysis techniques for quantifying pore-scale structure and processes in subsurface porous medium systems. Advances in Water Resources 51, 217–246. https://doi.org/10.1016/j.advwatres.2012.07.018

Zhao, B., MacMinn, C.W., Primkulov, B.K., Chen, Y., Valocchi, A.J., Zhao, J., Kang, Q., Bruning, K., McClure, J.E., Miller, C.T., Fakhari, A., Bolster, D., Hiller, T., Brinkmann, M., Cueto-Felgueroso, L., Cogswell, D.A., Verma, R., Prodanović, M., Maes, J., Geiger, S., Vassvik, M., Hansen, A., Segre, E., Holtzman, R., Yang, Z., Yuan, C., Chareyre, B., Juanes, R., 2019. Comprehensive comparison of pore-scale models for multiphase flow in porous media. Proceedings of the National Academy of Sciences 116, 13799–13806. https://doi.org/10.1073/pnas.1901619116